

Communication

Tailoring Ni and $\text{Sr}_2\text{Mg}_{0.25}\text{Ni}_{0.75}\text{MoO}_{6-\delta}$ Cermet Compositions for Designing the Fuel Electrodes of Solid Oxide Electrochemical Cells

Lubov S. Skutina ^{1,2,*}, Aleksey A. Vylkov ^{1,2}, Dmitry K. Kuznetsov ², Dmitry A. Medvedev ^{1,2,*} 
and Vladimir Ya. Shur ² 

¹ Laboratory of Electrochemical Devices Based on Solid Oxide Proton Electrolytes, Institute of High Temperature Electrochemistry, 620137 Yekaterinburg, Russia; aleksey.vylkov@urfu.ru

² Ural Federal University, 620002 Yekaterinburg, Russia; dimak@urfu.ru (D.K.K.); vladimir.shur@urfu.ru (V.Y.S.)

* Correspondence: lubov.skutina@yandex.ru (L.S.S.); dmitrymedv@mail.ru (D.A.M.)

Received: 12 June 2019; Accepted: 20 June 2019; Published: 21 June 2019



Abstract: The design of new electrode materials for solid oxide electrochemical cells, which are stable against redox processes as well as exhibiting carbon/sulphur tolerance and high electronic conductivity, is a matter of considerable current interest as a means of overcoming the disadvantages of traditional Ni-containing cermets. In the present work, composite materials having the general formula $(1-x)\text{Sr}_2\text{Mg}_{0.25}\text{Ni}_{0.75}\text{MoO}_{6-\delta} + x\text{NiO}$ (where $x = 0, 15, 30, 50, 70$ and 85 mol.%) were successfully prepared to be utilised in solid oxide fuel cells. A detailed investigation of the thermal, electrical, and microstructural properties of these composites, along with their phase stability in oxidising and reducing atmospheres, was carried out. While possessing low thermal expansion coefficient (TEC) values, the composites having low Ni content (15 mol.%–70 mol.%) did not satisfy the requirement of high electronic conductivity. Conversely, the $15\text{Sr}_2\text{Mg}_{0.25}\text{Ni}_{0.75}\text{MoO}_{6-\delta} + 85\text{NiO}$ samples demonstrated very high electrical conductivity (489 S cm^{-1} at 850°C in wet H_2) due to well-developed Ni-based networks, and no deterioration of thermal properties (TEC values of $15.4 \times 10^{-6} \text{ K}^{-1}$ in air and $14.5 \times 10^{-6} \text{ K}^{-1}$ in 50% H_2/Ar ; linear expansion behaviour in both atmospheres). Therefore, this material has potential for use as a component of a fuel cell electrode system.

Keywords: SOFCs; fuel electrodes; double perovskite; thermal expansion; composite materials

1. Introduction

Solid oxide fuel cells (SOFC) are electrochemical devices capable of converting hydrogen and more readily available carbon-containing fuels into electricity with high efficiency and low emissions [1–4]. Traditional SOFC systems based on yttria-stabilised zirconia (YSZ) electrolytes operate at very high (more than 800°C) temperatures required for reaching the sufficient performance [5,6]. However, such high temperatures impede the commercialisation of SOFCs due to the rapid component degradation associated with chemical (interdiffusion, chemical reactivity) and microstructural (electrolyte recrystallisation, electrode particle agglomeration, functional material delamination) factors [7–10]. While the degradation issue can be effectively tackled by designing low- and intermediate-temperature SOFCs, new challenges emerge in the course of developing the high-performance materials on which they are based.

Although typical Ni-based cermets are commonly used for SOFC anodes due to their excellent electrocatalytic properties [11–13], they have significant disadvantages associated with reduction-oxidation (redox) cycling instability and degradation due to the agglomeration of Ni particles occurring at high temperatures. Moreover, sulphur poisoning and carbon coking on the Ni-based

anode surface are serious problems when SOFCs are used with hydrocarbon fuels [14]. In this regard, considerable efforts have been made for the development of alternative anode materials with good catalytic activity combined with high tolerance to sulphide(s) formation and carbon deposition [15–19].

Recently, much attention has been paid to alternative systems based on strontium molybdates with the general formula $\text{Sr}_2\text{MMoO}_{6-\delta}$ ($\text{M} = \text{Mg}, \text{Mn}, \text{Fe}, \text{Co}, \text{Ni}$) [20–22]. According to an analysis of the literature, these materials perform well for the catalytic partial oxidation of methane [23–26] and have excellent coking and sulphur resistance characteristics [27–30]. However, these compounds have yet to be extensively employed due to their redox instability [20,21] or low electrical conductivity [28].

It is well-known that the functional properties of the basic materials can be improved using the doping method. For example, when evaluated for use as SOFC anode materials, the complex oxides of the $\text{Sr}_2\text{Ni}_{1-y}\text{Mg}_y\text{MoO}_{6-\delta}$ (SNMM) system showed better stability in both oxidising and reducing atmospheres compared with the basic members of the SNMM system, i.e., $\text{Sr}_2\text{MgMoO}_{6-\delta}$ and $\text{Sr}_2\text{NiMoO}_{6-\delta}$ [31–33]. At the same time, the transport properties of the SNMM materials ($0 < y < 1$) remained unsatisfactory. A modification (composite preparation) method can be used simultaneously alongside a doping approach in order to improve the conductivity of such compounds. In our previous work, we proposed adding a SrMoO_4 impurity phase, passing into a well-conducting SrMoO_3 phase in a reducing atmosphere [34]. Such an addition underpinned the design of the new SNMM– SrMoO_4 (and SNMM– SrMoO_3 in reducing form) cer-cer composite materials exhibiting excellent chemical and redox stability as well as improved transport properties ($>50 \text{ S cm}^{-1}$ at 600°C).

Another possible approach to optimising the properties of Mo-based oxides consists of the creation of cermets (ceramic-metal composite materials) [35,36]. For example, according to results of a study carried out by Niu et al., [35] Pd-impregnation of $\text{Sr}_{1.9}\text{VMoO}_{6+\delta}$ resulted in a decrease in polarisation resistance at the electrode due to an improvement in the charge-transfer process. Xiao et al. [36] reported a similar effect for the $\text{Sr}_2\text{Fe}_{1.5}\text{Mo}_{0.5}\text{O}_{6-\delta}$ fuel electrodes modified by a small amount of dispersed Ni phase. Despite the ostensive attractiveness of described impregnation/infiltration methods [37,38], the electrocatalytic activity of electrodes modified in this way tends to reduce over time due to a gradual dissolution of nanoparticles in the main backbone phase, leading to a decrease in the electrochemically active area.

Taking into account the mentioned drawbacks, we designed a new cermet composite system, $(1-x)\text{Sr}_2\text{Mg}_{0.25}\text{Ni}_{0.75}\text{MoO}_{6-\delta} + x\text{NiO}$, with a wide variation in NiO concentration ($15 \leq x, \text{mol.}\% \leq 85$). Particular attention was paid to studying the effect of second phase addition on the phase relation and microstructural features, as well as the thermomechanical and electrical characteristics depending on the oxidised and reduced form of the obtained composites.

2. Materials and Methods

2.1. Materials Preparation

To prepare the $(1-x)\text{Sr}_2\text{Mg}_{0.25}\text{Ni}_{0.75}\text{MoO}_{6-\delta} + x\text{NiO}$ composite materials, the $\text{Sr}_2\text{Mg}_{0.25}\text{Ni}_{0.75}\text{MoO}_{6-\delta}$ complex oxide was first synthesised using the glycine-nitrate synthesis method and then mechanically mixed with the NiO powder.

The details of the synthesis of the $\text{Sr}_2\text{Mg}_{0.25}\text{Ni}_{0.75}\text{MoO}_{6-\delta}$ material selected on the basis of works [31,34] are as follows. The $(\text{NH}_4)_6\text{Mo}_7\text{O}_{24}\cdot 4\text{H}_2\text{O}$, SrCO_3 , MgO and NiO powders used as starting components had a purity of not less than 99% (sigma-Aldrich production). SrCO_3 , MgO and NiO powders were measured according to a strictly required ratio and then dissolved in dilute nitric acid. Following the complete dissolution of these powders, glycerin as a chelating agent was added in a mole ratio of 1:2 with respect to the total metal cations of the target composition; then an aqua solution of ammonium molybdate with the known Mo-content (determined by the thermogravimetric analysis) was also added. The obtained transparent solution was treated at 250°C to provide pyrolysis. During this procedure, water evaporation, gelatinous mass formation, self-ignition, and the production of a highly dispersed powder were consistently observed. This powder was

then calcined at 800 °C (2 h) in order to remove organic or carbon compounds, pre-synthesised at 1100 °C (5 h) to reach phase crystallisation and finally synthesised at 1100 °C (5 h) to ensure excellent chemical homogeneity. The powder was thoroughly milled (using an agate pestle and mortar) after each temperature treatment. The obtained $\text{Sr}_2\text{Mg}_{0.25}\text{Ni}_{0.75}\text{MoO}_{6-\delta}$ material was mixed with the NiO powder (Pulverisette 7 planetary mill, 400 rpm, 30 min); the concentration of NiO was varied from 15 to 85 mol.%. The composite materials were pressed at 250 MPa to form pellets ($3 \times 5 \times 15$ cm), which were then sintered at 1350 °C for 2 h.

2.2. Materials Characterization

The $(1-x)\text{Sr}_2\text{Mg}_{0.25}\text{Ni}_{0.75}\text{MoO}_{6-\delta} + x\text{NiO}$ composite materials were characterised by X-ray diffraction (XRD) analysis using a Rigaku D/MAX-2200VL/PC diffractometer [39]. The analysis was performed using $\text{Cu-K}\alpha$ radiation in an angle range of 20–75° with a step of 0.02° and a scan rate of 3 min^{-1} . The XRD analysis was also performed for the samples of $(1-x)\text{Sr}_2\text{Mg}_{0.25}\text{Ni}_{0.75}\text{MoO}_{6-\delta} + x\text{Ni}$ reduced in pure H_2 at 800 °C for 5 h.

The morphology of the sintered and reduced ceramic materials was studied by scanning electron microscopy (SEM, Merlin, Carl Zeiss [40]) equipped with an X-Max Extreme (Oxford Instruments) detector for energy-dispersive X-ray (EDX) spectroscopy.

The thermal behaviour and thermal expansion coefficients (TECs) of the materials were evaluated using a DIL 402 C dilatometer (Netzsch GmbH). The experiments were carried out within a temperature range of 100–800 °C in both air and 50% H_2 /Ar gas media.

The electrical conductivity characterisation for the reduced samples was carried out using a four-point DC technique in wet hydrogen atmospheres. The temperature and conductivity were automatically controlled using a microprocessor system Zirconia-318 [41].

3. Results and Discussion

3.1. Phase Relation

In order to investigate a chemical stability and compatibility of the $\text{Sr}_2\text{Mg}_{0.25}\text{Ni}_{0.75}\text{MoO}_{6-\delta}$ double perovskite with NiO, an XRD study was carried out for both as-sintered and reduced samples (Figure 1 and Figure S1). As can be seen, the XRD patterns contain reflections of the main double perovskite structure, NiO and trace amounts of a SrMoO_4 phase (Figure 1a) for all the materials obtained following the sintering procedure. It should be noted that the existence of the latter is a characteristic feature for compounds with a general A_2BMoO_6 formula prepared under oxidising conditions [42–44].

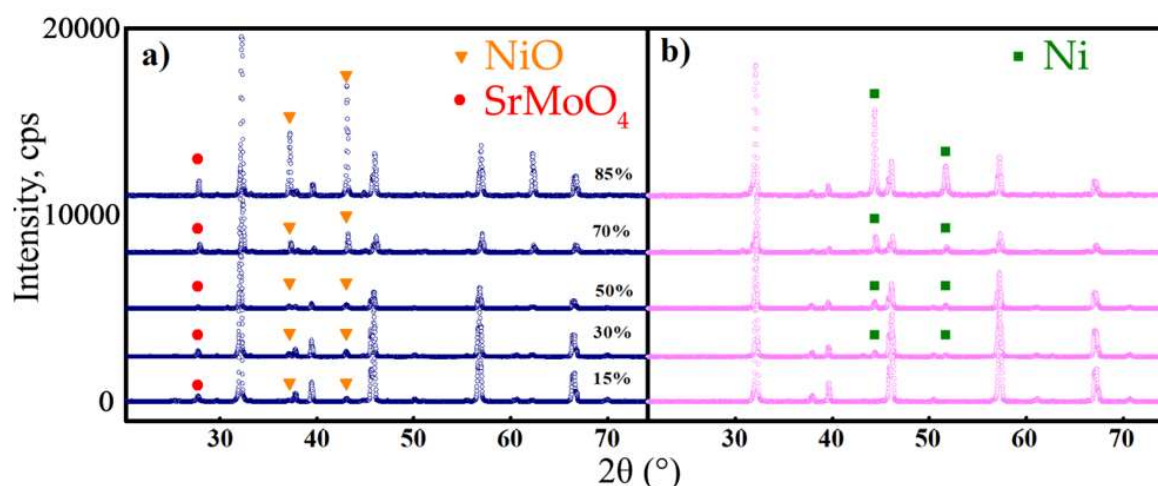


Figure 1. XRD data for the $(1-x)\text{Sr}_2\text{Mg}_{0.25}\text{Ni}_{0.75}\text{MoO}_{6-\delta} + x\text{NiO}$ composite materials obtained after (a) sintering in air at 1350 °C and (b) reducing in 50% H_2 /Ar mixture at 800 °C.

Following exposure in H_2 , no $SrMoO_4$ phase (or reduced $SrMoO_3$ product) was found: almost all the samples represented two-phase systems consisting of the double perovskite and Ni compounds (Figure 1b). The most likely explanation for the disappearance of the $SrMoO_3$ impurity is its dissolution in the basic phase. Interestingly, the reduced material of 85% $Sr_2Mg_{0.25}Ni_{0.75}MoO_{6-\delta}$ + 15% Ni nominal composition was found to be single-phase. This can be attributed either to a complete co-dissolution of $SrMoO_3$ and Ni or insufficient diffractometer resolution, which only permits detection of phases in concentrations greater than 3 wt.%. In this reduced composite material, the weight fraction of Ni is equal to ~2.4 wt.%.

3.2. Thermal Behaviour

In order to satisfy thermo-mechanical criteria as well as suppress the strain and stress during operation of the electrochemical SOFC devices at elevated temperatures, the thermal expansion behaviour of the oxides needs to be evaluated. In the case of new anode materials, their thermal behaviour was verified not only for the oxidising but also for the reducing conditions in which they operate.

Figure 2 and Figure S2 show the dilatometry curves of the oxidised $(1-x)Sr_2Mg_{0.25}Ni_{0.75}MoO_{6-\delta}$ + $xNiO$ ceramic composites and their reduced products. Moreover, the pure NiO sample was also prepared and included in the general system of the composites. As can be seen, the curves for pure NiO and Ni show slope changes in their linear trend in air as well as in 50% H_2/Ar mixture, respectively, indicating the presence of undesirable phase transitions. Conversely, all composites exhibit a linear behaviour of thermal expansion in the whole studied temperature range without any detectable curvature.

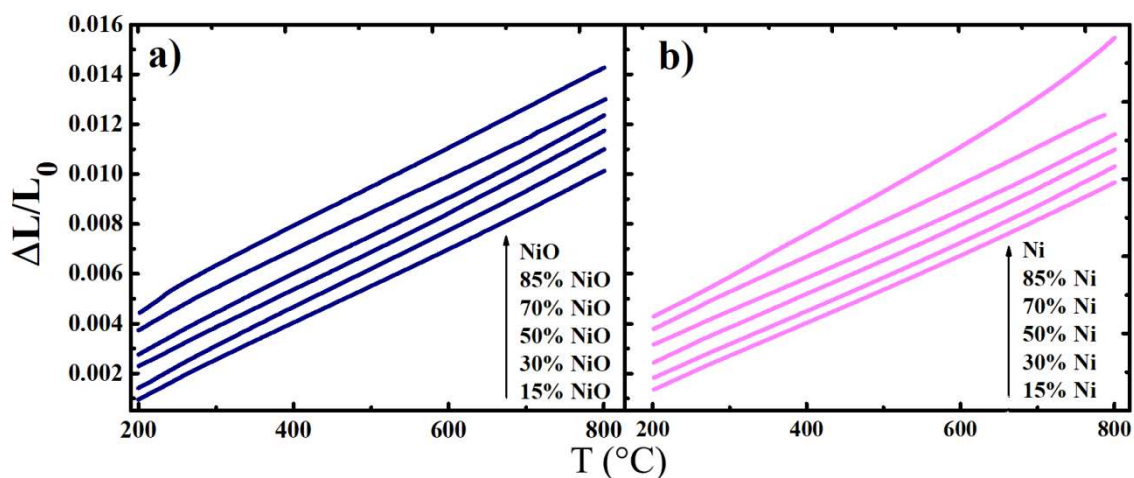


Figure 2. Thermal expansion curves of the $(1-x)Sr_2Mg_{0.25}Ni_{0.75}MoO_{6-\delta}$ + $xNiO$ composites and NiO oxide between 200 and 800 °C (a) in the air (b) in 50% H_2/Ar mixture.

From dilatometry dependencies, the average thermal expansion coefficient (TEC) values were calculated as follows:

$$\alpha = \frac{1}{L_0} \cdot \frac{d\Delta L}{dT}, \quad (1)$$

where L_0 is the length of the initial sample and ΔL is the relative length variation at temperature change (T).

According to Table 1, the average TECs values changed insignificantly when varying the NiO concentration in the oxidised samples and Ni concentration in the reduced samples; they belong to the ranges of $(15.3 \pm 0.3) \cdot 10^{-6}$ and $(14.2 \pm 0.4) \cdot 10^{-6} K^{-1}$, respectively. As can be seen, the individual $Sr_2Mg_{0.25}Ni_{0.75}MoO_{6-\delta}$ material demonstrated the lowest TEC value in air and a medium value in wet hydrogen, while NiO and Ni phase were characterised by the highest TECs in the

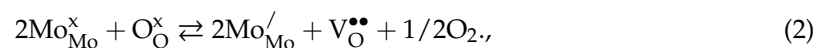
corresponding atmospheres. It can be assumed that TECs in the $(1-x)\text{Sr}_2\text{Mg}_{0.25}\text{Ni}_{0.75}\text{MoO}_{6-\delta} + x\text{NiO}$ or $(1-x)\text{Sr}_2\text{Mg}_{0.25}\text{Ni}_{0.75}\text{MoO}_{6-\delta} + x\text{Ni}$ systems should change monotonically with a gradual increase in x . However, this assumption was not confirmed – at least for $15 \leq x, \text{mol.}\% \leq 70$ – since a percolation barrier ($\sim 30 \text{ vol.}\%$ and $70 \text{ vol.}\%$) was not achieved at these mole concentrations. In other words, the thermal behaviour and TECs values were determined by the backbone phase of the double perovskite.

Table 1. The average TECs of the composite materials in air (α_{ox}) and 50% H_2/Ar (α_{red}) atmospheres. These values were calculated from dilatometry curves obtained in cooling mode.

x in $(1-x)\text{Sr}_2\text{Mg}_{0.25}\text{Ni}_{0.75}\text{MoO}_{6-\delta} + x\text{NiO}$	$\alpha_{\text{ox}} \cdot 10^6, \text{K}^{-1}$	x in $(1-x)\text{Sr}_2\text{Mg}_{0.25}\text{Ni}_{0.75}\text{MoO}_{6-\delta} + x\text{Ni}$	$\alpha_{\text{red}} \cdot 10^6, \text{K}^{-1}$
0	14.6 [34]	0	14.0 [34]
15	15.1	15	13.8
30	15.6	30	13.9
50	15.6	50	14.0
70	15.6	70	13.9
85	15.4	85	14.5
100	23.1 (200–235 °C) 16.6 (235–800 °C)	100	17.0 (200–580 °C) 21.2 (580–800 °C)

With regard to the type of atmosphere, it can be revealed that the calculated TEC values for the composite materials were slightly lower in 50% H_2/Ar than those obtained in air. The difference in the observed TECs is caused by those elements capable of changing their oxidation state. Therefore, the following factors occur for the studied system:

1. The molybdenum ions reduction, $\text{Mo}^{6+} \rightarrow \text{Mo}^{5+}$ (Equation (2)), results in a slight increase in the average ionic radii of elements occupied B-position of the $\text{A}_2\text{BB}'\text{O}_6$ structure, since $r(\text{Mo}^{6+}) = 0.59 \text{ \AA}$ and $r(\text{Mo}^{5+}) = 0.61 \text{ \AA}$ [45].



2. Together with a minor strain in cationic sublattice, the dimension change (contraction) in the anionic sublattice is estimated to be more pronounced due to oxygen desorption ($r_{\text{O}_x} = 1.40 \text{ \AA}$, $r_{\text{V}_{\text{O}}^{\cdot\cdot}} = 1.18 \text{ \AA}$ [46,47]) occurring as a compensation of the Mo-ions reduction process. Here, the ionic radii values are provided using the Shannon's system [48].
3. NiO undergoes a complete reduction in a hydrogen atmosphere until the formation of a Ni metallic phase. The volume changes during this reduction amount $\sim 40\%$ [49].

A comparison of the abovementioned factors allows two different conclusions to be revealed. The first of these consists in the fact that differences in α_{ox} and α_{red} are predominantly caused by the contraction of the anionic sublattice. Such a contraction along with the Mo-ions reduction results in a more packed lattice, for which the vibration amplitude can be lowered due to strengthening the M – O (M = Fe, Mo) ionic bonds. This is in accordance with shifting the XRD characteristic reflexes of the reduced materials to higher angles in comparison with the oxidised materials (Figure S1). The second conclusion implies that the thermal behaviour of the materials is not determined by NiO or Ni phase, with the exception of the composite having $x = 85$, which had a higher TEC value compared with the other composites. The second conclusion is also confirmed by the fact that pure NiO and Ni phases exhibit non-monotonic expansion and very high TEC values (Table 1) due to phase transitions [50].

3.3. Conductivity Behaviour

The total conductivity of the $(1-x)\text{Sr}_2\text{Mg}_{0.25}\text{Ni}_{0.75}\text{MoO}_{6-\delta} + x\text{Ni}$ ceramic materials in wet hydrogen atmosphere is shown in Figure 3. The composites having a low Ni concentration ($x = 15, 30$ and 50) displayed virtually the same conductivity level. As mentioned above, these composites are comprised

of a Mo-based framework in which the Ni-based phase is statistically distributed. Therefore, no continuous metallic phase is formed for these objects, causing their fairly low conductivity levels in accordance with the transport properties of some double molybdates (Table S1, [27,51–53]). When the Ni concentration was increased, the conductivity tended to increase considerably, up to $\sim 2.7 \text{ S cm}^{-1}$ at $800 \text{ }^\circ\text{C}$ (Table 2) and then to more than 450 S cm^{-1} at the same temperature. Moreover, the conducting behaviour of the composites was also quite varied, explained in terms of a change in the slope of conductivity dependencies in Arrhenius coordinates. This again indicates that the percolation effect is invoked when the nickel content varies between 70 mol.% and 85 mol.%.

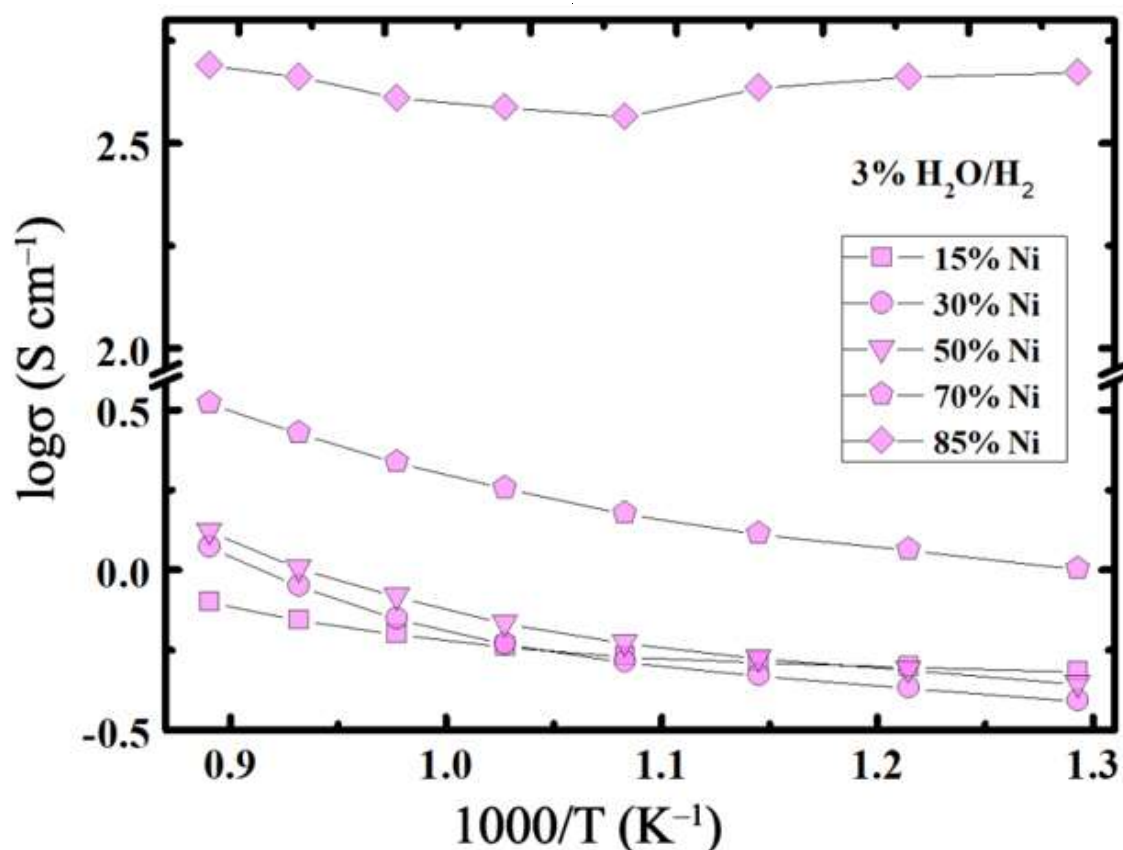


Figure 3. Temperature dependences of conductivity for the $(1-x)\text{Sr}_2\text{Mg}_{0.25}\text{Ni}_{0.75}\text{MoO}_{6-\delta} + x\text{Ni}$ composites in $3\%\text{H}_2\text{O}/\text{H}_2$ atmosphere.

Table 2. Electrical conductivity (at $800 \text{ }^\circ\text{C}$) and activation energy value of the $(1-x)\text{Sr}_2\text{Mg}_{0.25}\text{Ni}_{0.75}\text{MoO}_{6-\delta} + x\text{Ni}$ composite materials in $3\%\text{H}_2\text{O}/\text{H}_2$ atmosphere.

x , Ni content	σ , S cm^{-1}	E_a , eV
15	0.79	0.11 (500–650 $^\circ\text{C}$), 0.23 (650–800 $^\circ\text{C}$)
30	1.18	0.18 (500–650 $^\circ\text{C}$), 0.33 (650–800 $^\circ\text{C}$)
50	1.01	0.19 (500–650 $^\circ\text{C}$), 0.30 (650–800 $^\circ\text{C}$)
70	2.66	0.23 (500–650 $^\circ\text{C}$), 0.43 (650–800 $^\circ\text{C}$)
85	458	– (500–600 $^\circ\text{C}$), 0.21 (650–800 $^\circ\text{C}$)

3.4. Microstructural Features

In order to understand the thermal and electrical behaviours of the materials developed, they were characterised by SEM analysis. The corresponding images for the as-sintered and reduced composite samples are presented in Figures 4 and 5, respectively. Analysing the data obtained for the oxidised

$(1-x)\text{Sr}_2\text{Mg}_{0.25}\text{Ni}_{0.75}\text{MoO}_{6-\delta} + x\text{NiO}$ materials (Figure 4), it can be noted that they were rather porous (10–20 vol.%) and consisted of a grain-based structure with well distinguished grain boundaries at low x values, while more dense samples with a lower porosity (5 vol.%–10 vol.%) and solid structure were formed at high x values. Since the composite materials were multi-phase (Figure 1a), different micro- and sub-micro sediments were detected along with the grains (Figure S3).

When the composites were reduced, their ceramic parameters were changed (Figure 5). In detail, all the samples exhibited a crystallite structure composed of grains of two (Ni- and molybdate-based) phases and large amounts of pores (20 vol.%–30 vol.%). The latter was mostly caused by the mentioned volume changes during $\text{NiO} \rightarrow \text{Ni}$ reduction. The results of the EDX spectroscopy showed that the Ni metallic phase was initially located as individual particles and then formed a continuous network with a gradual increase of nickel concentration. Only in the case of 85 mol.% Ni in the composite system does the volume fraction of this metal exceed the percolation effect, resulting in the sharp changes in TECs (Table 1) and a dramatic increase in electronic conductivity (Figure 3).

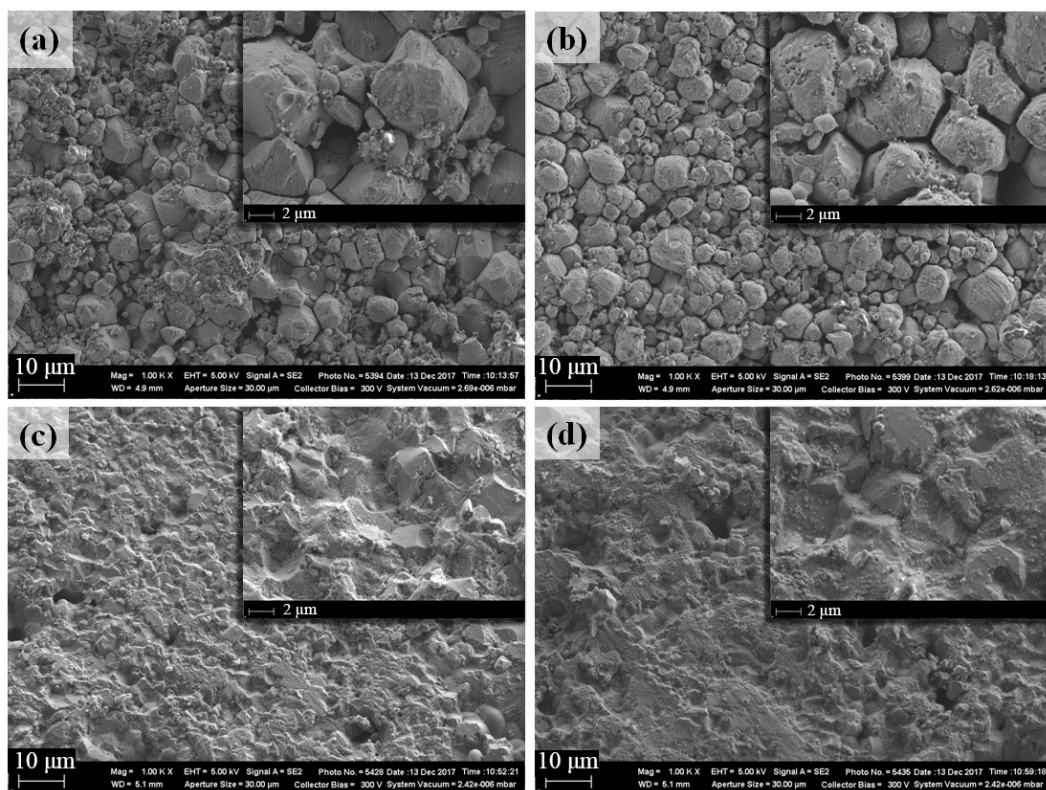


Figure 4. Surface morphology images for the as-sintered $(1-x)\text{Sr}_2\text{Mg}_{0.25}\text{Ni}_{0.75}\text{MoO}_{6-\delta} + x\text{NiO}$ ceramic materials: $x = 15$ (a), $x = 30$ (b), $x = 70$ (c) and $x = 85$ (d).

4. Conclusions

In the present work, new $(1-x)\text{Sr}_2\text{Mg}_{0.25}\text{Ni}_{0.75}\text{MoO}_{6-\delta} + x\text{NiO}$ composite powders with different NiO mole concentrations (15%, 30%, 50%, 70%, and 85%) were successfully obtained. Their phase composition, microstructure, thermal, and electrical properties were thoroughly studied in oxidising (air) and reducing (wet H_2) atmospheres.

From the results obtained, the following conclusions can be made:

1. All the materials were stable in both oxidising and reducing atmospheres. The reduced samples were found to comprise dual-phase materials, while an impurity SrMoO_4 phase was detected along with two target phases for the oxidised samples.

- Thermal expansion of the studied composite materials was linear over the entire temperature range (200–800 °C); the calculated TECs values remained more or less consistent with a variation in composition, decreasing from the oxidised to the reduced samples.
- The total conductivity of the reduced composites did not exceed 3 S cm^{-1} at 800 °C at $15 \leq x$, $\text{mol.}\% \leq 70$; whereas, it amounts to 450 S cm^{-1} for $x = 85 \text{ mol.}\%$ at the same temperature.

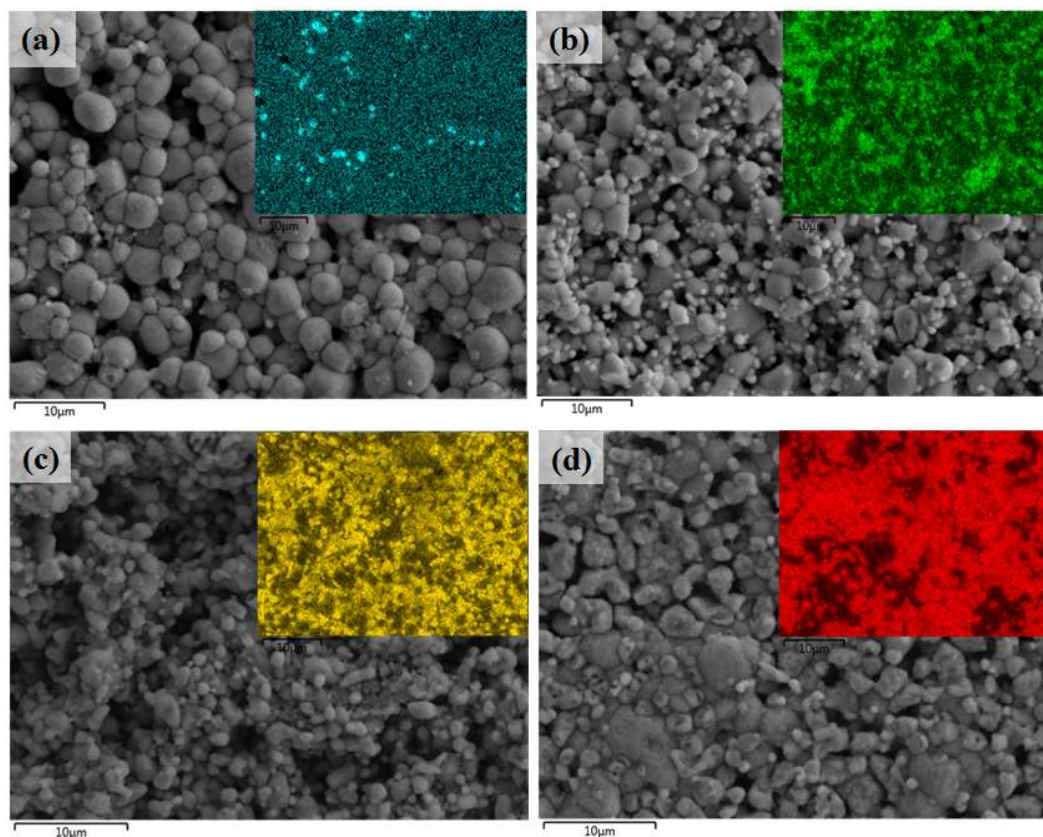


Figure 5. Images of the surface morphology and map of Ni-distribution for the reduced $(1-x)\text{Sr}_2\text{Mg}_{0.25}\text{Ni}_{0.75}\text{MoO}_{6-\delta} + x\text{Ni}$ ceramic materials: $x = 15$ (a), $x = 30$ (b), $x = 70$ (c) and $x = 85$ (d).

The $15\text{Sr}_2\text{Mg}_{0.25}\text{Ni}_{0.75}\text{MoO}_{6-\delta} + 85\text{NiO}$ composite material and its reduced product have potential for use in a fuel electrode system due to their high conductivity and tolerance to meaningful dimensional changes. It should be noted that such a composite is characterised by the high amount of nickel, the presence of which might lead to sulfidation and carbonization [3]; nevertheless, the co-presence of the double molybdate phase is assumed to promote S-desorption and inhibit coke formation [54,55]. Moreover, its electrochemical behaviour should be verified, for example, using electrochemical impedance spectroscopy, which will be addressed in future research.

Supplementary Materials: The following are available online at <http://www.mdpi.com/1996-1073/12/12/2394/s1>, Figure S1: Comparison of the XRD data of the $50\text{Sr}_2\text{Mg}_{0.25}\text{Ni}_{0.75}\text{MoO}_{6-\delta} + 50\text{NiO}$ and $50\text{Sr}_2\text{Mg}_{0.25}\text{Ni}_{0.75}\text{MoO}_{6-\delta} + 50\text{Ni}$ composites, Figure S2: Comparison of the relative dimension changes of $50\text{Sr}_2\text{Mg}_{0.25}\text{Ni}_{0.75}\text{MoO}_{6-\delta} + 50\text{NiO}$ and $50\text{Sr}_2\text{Mg}_{0.25}\text{Ni}_{0.75}\text{MoO}_{6-\delta} + 50\text{Ni}$, Figure S3: Images of the surface morphology for the as-sintered $(1-x)\text{Sr}_2\text{Mg}_{0.25}\text{Ni}_{0.75}\text{MoO}_{6-\delta} + x\text{NiO}$ ceramic materials at high magnification, Table S1: Total conductivity of Mg-based molybdate materials with a double perovskite structure at 800 °C in reducing atmospheres.

Author Contributions: Conceptualization, L.S.S. and A.A.V.; methodology, D.A.M.; validation, D.K.K. and V.Y.S.; formal analysis, D.A.M.; investigation, L.S.S.; resources, D.K.K. and V.Y.S.; writing—original draft preparation, L.S.S. and D.A.M.; writing—review and editing, D.A.M.; visualization, L.S.S.; supervision, A.A.V.; project administration, L.S.S.; funding acquisition, L.S.S.

Funding: This work is supported by the Russian Foundation for Basic Research (project no. 18-33-00544).

Acknowledgments: The authors thank to the Shared Access Centre “Composition of compounds” (Institute of High Temperature Electrochemistry) and the Ural Center for Shared Use “Modern nanotechnology” (Ural Federal University) for carrying out the XRD and SEM analyses.

Conflicts of Interest: The authors declare no conflict of interest.

References

1. Ramadhani, F.; Hussain, M.A.; Mokhlis, H.; Hajimolana, S. Optimization strategies for Solid Oxide Fuel Cell (SOFC) application: A literature survey. *Renew. Sustain. Energy Rev.* **2017**, *76*, 460–484. [[CrossRef](#)]
2. Abdalla, A.M.; Hossain, S.; Azad, A.T.; Petra, P.M.I.; Begum, F.; Eriksson, S.G.; Azad, A.K. Nanomaterials for solid oxide fuel cells: A review. *Renew. Sustain. Energy Rev.* **2018**, *82*, 353–368. [[CrossRef](#)]
3. Mahato, N.; Banerjee, A.; Gupta, A.; Omar, S.; Balani, K. Progress in material selection for solid oxide fuel cell technology: A review. *Prog. Mater. Sci.* **2015**, *72*, 141–337. [[CrossRef](#)]
4. Ruiz-Morales, J.C.; Tarancón, A.; Canales-Vázquez, J.; Méndez-Ramos, J.; Hernández-Afonso, L.; Acosta-Mora, P.; Marín Rueda, J.R.; Fernández-González, R. Three dimensional printing of components and functional devices for energy and environmental applications. *Energy Environ. Sci.* **2017**, *10*, 846–859. [[CrossRef](#)]
5. Minh, N.Q. Solid oxide fuel cell technology—features and applications. *Solid State Ion.* **2004**, *174*, 271–277. [[CrossRef](#)]
6. Yamamoto, O. Solid oxide fuel cells: Fundamental aspects and prospects. *Electrochim. Acta* **2000**, *45*, 2423–2435. [[CrossRef](#)]
7. Yang, Z.; Guo, M.; Wang, N.; Ma, C.; Wang, J.; Han, M. A short review of cathode poisoning and corrosion in solid oxide fuel cell. *Int. J. Hydrogen Energy* **2014**, *42*, 24948–24959. [[CrossRef](#)]
8. Chen, K.; Jiang, S.P. Review—Materials degradation of solid oxide electrolysis cells. *J. Electrochem. Soc.* **2016**, *163*, F3070–F3083. [[CrossRef](#)]
9. Torrell, M.; Morata, A.; Kayser, P.; Kendall, M.; Kendall, K.; Tarancón, A. Performance and long term degradation of 7 W micro-tubular solid oxide fuel cells for portable applications. *J. Power Sources* **2018**, *285*, 439–448. [[CrossRef](#)]
10. Téllez, H.; Druce, J.; Ishihara, T.; Kilner, J.A. Effects of microstructure on surface segregation: Role of grain boundaries. *ECS Trans.* **2016**, *72*, 57–69. [[CrossRef](#)]
11. Kim, S.-D.; Moon, H.; Hyun, S.-H.; Moon, J.; Kim, J.; Lee, H.-W. Ni-YSZ cermet anode fabricated from NiO-YSZ composite powder for high-performance and durability of solid oxide fuel cells. *Solid State Ion.* **2007**, *178*, 1304–1309. [[CrossRef](#)]
12. Faes, A.; Hessler-Wyser, A.; Zryd, A. A review of RedOx cycling of solid oxide fuel cells anode. *Membranes* **2012**, *2*, 585–664. [[CrossRef](#)]
13. Mogensen, M.; Høgh, J.; Hansena, K.V.; Jacobsen, T. A critical review of models of the H₂/H₂O/Ni/SZ electrode kinetics. *ECS Trans.* **2007**, *7*, 1329–1338.
14. Khan, M.S.; Lee, S.-B.; Song, R.-H.; Lee, J.-W.; Lim, T.-H.; Park, S.-J. Fundamental mechanisms involved in the degradation of nickel–yttria stabilized zirconia (Ni–YSZ) anode during solid oxide fuel cells operation: A review. *Ceram. Int.* **2016**, *42*, 35–48. [[CrossRef](#)]
15. Rafique, M.; Nawaz, H.; Shahid Rafique, M.; Bilal Tahir, M.; Nabi, G.; Khalid, N.R. Material and method selection for efficient solid oxide fuel cell anode: Recent advancements and reviews. *Int. J. Energy Res.* **2019**, *43*, 2423–2446. [[CrossRef](#)]
16. Acosta, M.; Baiutti, F.; Tarancón, A.; MacManus-Driscoll, J.L. Nanostructured materials and interfaces for advanced ionic electronic conducting oxides. *Adv. Mater. Interfaces* **2019**. [[CrossRef](#)]
17. Wei, K.; Wang, X.; Budiman, R.A.; Kang, J.; Lin, B.; Zhou, F.; Ling, Y. Progress in Ni-based anode materials for direct hydrocarbon solid oxide fuel cells. *J. Mater. Sci.* **2018**, *53*, 8747–8765. [[CrossRef](#)]
18. Istomin, S.Ya.; Kotova, A.I.; Lyskov, N.V.; Mazo, G.N.; Antipov, E.V. Pr₅Mo₃O_{16+δ}: A new anode material for solid oxide fuel cells. *Russ. J. Inorg. Chem.* **2018**, *63*, 1291–1296. [[CrossRef](#)]
19. Istomin, S.Ya.; Morozov, A.V.; Abdullayev, M.M.; Batuk, M.; Hadermann, J.; Kazakov, S.M.; Sobolev, A.V.; Presniakov, I.A.; Antipov, E.V. High-temperature properties of (La,Ca)(Fe,Mg,Mo)O_{3-δ} perovskites as prospective electrode materials for symmetrical SOFC. *J. Solid State Chem.* **2018**, *258*, 1–10. [[CrossRef](#)]

20. Vasala, S.; Lehtimäki, M.; Huang, Y.H.; Yamauchi, H.; Goodenough, J.B.; Karppinen, M. Degree of order and redox balance in B-site ordered double-perovskite oxides $\text{Sr}_2\text{MMoO}_{6-\delta}$ (M = Mg, Mn, Fe, Co, Ni, Zn). *J. Solid State Chem.* **2010**, *183*, 1007–1012. [[CrossRef](#)]
21. Bernuy-Lopez, C.; Allix, M.; Bridges, C.A.; Claridge, J.B.; Rosseinsky, M.J. $\text{Sr}_2\text{MgMoO}_6$: Structure, phase stability and cation site order control of reduction. *Chem. Mater.* **2007**, *19*, 1035–1043. [[CrossRef](#)]
22. Wei, T.; Ji, Y.; Meng, X.; Zhang, Y. $\text{Sr}_2\text{NiMoO}_{6-\delta}$ as anode material for LaGaO_3 -based solid oxide fuel cell. *Electrochem. Commun.* **2008**, *10*, 1369–1372. [[CrossRef](#)]
23. Li, C.; Wang, W.; Zhao, N.; Liu, Y.; He, B.; Hu, F.; Chen, C. Structure properties and catalytic performance in methane combustion of double perovskites $\text{Sr}_2\text{Mg}_{1-x}\text{Mn}_x\text{MoO}_{6-\delta}$. *Appl. Catal. B Environ.* **2010**, *102*, 78–84. [[CrossRef](#)]
24. Li, C.; Wang, W.; Xu, C.; Liu, Y.; He, B.; Chen, C. Double perovskite oxides $\text{Sr}_2\text{Mg}_{1-x}\text{Fe}_x\text{MoO}_{6-\delta}$ for catalytic oxidation of methane. *J. Nat. Gas Chem.* **2011**, *156*, 345–349. [[CrossRef](#)]
25. Wang, Z.; Tian, Y.; Li, Y. Direct CH_4 fuel cell using $\text{Sr}_2\text{FeMoO}_6$ as an anode material. *J. Power Sources* **2011**, *196*, 6104–6109. [[CrossRef](#)]
26. Escudero, M.; Gómez de Parada, I.; Fuerte, A.; Daza, L. Study of $\text{Sr}_2\text{Mg}(\text{Mo}_{0.8}\text{Nb}_{0.2})\text{O}_{6-\delta}$ as anode material for solid oxide fuel cells using hydrocarbons as fuel. *J. Power Sources* **2013**, *243*, 654–660. [[CrossRef](#)]
27. Howell, T.; Kuhnell, C.; Reitz, T. A_2MgMoO_6 (A = Sr, Ba) for use as sulfur tolerant anodes. *J. Power Sources* **2013**, *231*, 279–284. [[CrossRef](#)]
28. Zheng, K.; Swierczek, K.; Zając, W.; Klimkowicz, A. Rock salt ordered-type double perovskite anode materials for solid oxide fuel cells. *Solid State Ion.* **2014**, *257*, 9–16. [[CrossRef](#)]
29. Niu, B.; Jin, F.; Yang, X.; Feng, T.; He, T. Resisting coking and sulfur poisoning of double perovskite $\text{Sr}_2\text{TiFe}_{0.5}\text{Mo}_{0.5}\text{O}_{6-\delta}$ anode material for solid oxide fuel cells. *Int. J. Hydrogen Energy* **2018**, *43*, 3280–3290. [[CrossRef](#)]
30. Gwan, M.A.; Yun, J.W. Carbon tolerance effects of $\text{Sr}_2\text{NiMoO}_{6-\delta}$ as an alternative anode in solid oxide fuel cell under methane fuel condition. *J. Electroceramics* **2018**, *40*, 171–179. [[CrossRef](#)]
31. Filonova, E.A.; Dmitriev, A.S.; Pikalov, P.S.; Medvedev, D.A.; Pikalova, E.Yu. The structural and electrical properties of $\text{Sr}_2\text{Ni}_{0.75}\text{Mg}_{0.25}\text{MoO}_6$ and its compatibility with solid state electrolytes. *Solid State Ion.* **2014**, *262*, 365–369. [[CrossRef](#)]
32. Xie, Z.; Zhao, H.; Du, Z.; Chen, T.; Chen, N. Electrical, chemical, and electrochemical properties of double perovskite oxides $\text{Sr}_2\text{Mg}_{1-x}\text{Ni}_x\text{MoO}_{6-\delta}$ as anode materials for solid oxide fuel cells. *J. Phys. Chem. C* **2014**, *118*, 18853–18860. [[CrossRef](#)]
33. Sereda, V.V.; Tsvetkov, D.S.; Sednev, A.L.; Druzhinina, A.I.; Malyshkin, D.A.; Zuev, A.Y. Thermodynamics of $\text{Sr}_2\text{NiMoO}_6$ and $\text{Sr}_2\text{CoMoO}_6$ and their stability under reducing conditions. *Phys. Chem. Chem. Phys.* **2018**, *20*, 20108–20116. [[CrossRef](#)] [[PubMed](#)]
34. Skutina, L.S.; Vylkov, A.I.; Medvedev, D.A.; Filonova, E.A. Features of structural, thermal and electrical properties of Mo-based composite materials as fuel electrodes for high-temperature applications. *J. Alloys Compd.* **2017**, *705*, 854–861. [[CrossRef](#)]
35. Niu, B.; Jin, F.; Fu, R.; Feng, T.; Shen, Y.; Liu, J.; He, T. Pd-impregnated $\text{Sr}_{1.9}\text{VMoO}_{6+\delta}$ double perovskite as an efficient and stable anode for solid-oxide fuel cells operating on sulfur-containing syngas. *Electrochim. Acta* **2018**, *274*, 91–102. [[CrossRef](#)]
36. Xiao, G.; Chen, F. Ni modified ceramic anodes for direct-methane solid oxide fuel cells. *Electrochem. Commun.* **2011**, *13*, 57–59. [[CrossRef](#)]
37. Fan, L.; Zhu, B.; Sud, P.-C.; He, C. Nanomaterials and technologies for low temperature solid oxide fuel cells: Recent advances, challenges and opportunities. *Nano Energy* **2018**, *45*, 148–176. [[CrossRef](#)]
38. Ding, D.; Li, X.; Lai, S.Y.; Gerdes, K.; Liu, M. Enhancing SOFC cathode performance by surface modification through infiltration. *Energy Environ. Sci.* **2014**, *7*, 552–575. [[CrossRef](#)]
39. Available online: http://www.ihte.uran.ru/?page_id=3154 (accessed on 21 June 2019).
40. Available online: <https://nanocenter.urfu.ru/en> (accessed on 21 June 2019).
41. Available online: <https://zirconiaproject.wordpress.com/devices/zirconia-318/> (accessed on 21 June 2019).
42. Osinkin, D.A.; Zabolotskaya, E.V.; Kellerman, D.G.; Suntsov, A.Yu. The physical properties and electrochemical performance of Ca-doped $\text{Sr}_2\text{MgMoO}_{6-\delta}$ as perspective anode for solid oxide fuel cells. *J. Solid State Electrochem.* **2018**, *22*, 1209–1215. [[CrossRef](#)]

43. Filonova, E.A.; Russkikh, O.V.; Skutina, L.S.; Kochetova, N.A.; Korona, D.V.; Ostroushko, A.A. Influence of synthesis conditions on phase formation and functional properties of prospective anode material $\text{Sr}_2\text{Ni}_{0.75}\text{Mg}_{0.25}\text{MoO}_{6-\delta}$. *J. Alloys Compd.* **2018**, *748*, 671–678. [[CrossRef](#)]
44. Merkulov, O.V.; Markov, A.A.; Patrakeev, M.V.; Leonidov, I.A.; Shalaeva, E.V.; Tyutyunnik, A.P.; Kozhevnikov, V.L. Structural features and high-temperature transport in $\text{SrFe}_{0.7}\text{Mo}_{0.3}\text{O}_{3-\delta}$. *J. Solid State Chem.* **2018**, *258*, 447–452. [[CrossRef](#)]
45. Tsvetkov, D.S.; Ivanov, I.L.; Malyshkin, D.A.; Steparuk, A.S.; Zuev, A.Y. The defect structure and chemical lattice strain of the double perovskites $\text{Sr}_2\text{BMoO}_{6-\delta}$ (B = Mg, Fe). *Dalton Trans.* **2016**, *45*, 12906–12913. [[CrossRef](#)] [[PubMed](#)]
46. Bishop, S.R.; Marrocchelli, D.; Chatzichristodoulou, C.; Perry, N.H.; Mogensen, M.B.; Tuller, H.L.; Wachsmann, E.D. Chemical expansion: Implications for electrochemical energy storage and conversion devices. *Annu. Rev. Mater. Res.* **2014**, *44*, 205–239. [[CrossRef](#)]
47. Løken, A.; Ricote, S.; Wachowski, S. Thermal and chemical expansion in proton ceramic electrolytes and compatible electrodes. *Crystals* **2018**, *8*, 365. [[CrossRef](#)]
48. Shannon, R.D. Revised effective ionic radii and systematic studies of interatomic distances in halides and chalcogenides. *Acta Crystallogr.* **1976**, *32*, 751–767. [[CrossRef](#)]
49. Coors, W.G.; Manerbino, A. Characterization of composite cermet with 68 wt.% NiO and $\text{BaCe}_{0.2}\text{Zr}_{0.6}\text{Y}_{0.2}\text{O}_{3-\delta}$. *J. Membr. Sci.* **2011**, *376*, 50–55. [[CrossRef](#)]
50. Mori, M.; Yamamoto, T.; Itoh, H.; Inaba, H.; Tagawa, H. Thermal expansion of nickel-zirconia anodes in solid oxide fuel cells during fabrication and operation. *J. Electrochem. Soc.* **1998**, *145*, 1374–1381. [[CrossRef](#)]
51. Marrero-López, D.; Peña-Martínez, J.; Ruiz-Morales, J.C.; Gabás, M.; Núñez, P.; Aranda, M.A.G.; Ramos-Barrado, J.R. Redox behaviour, chemical compatibility and electrochemical performance of $\text{Sr}_2\text{MgMoO}_{6-\delta}$ as SOFC anode. *Solid State Ion.* **2010**, *180*, 1672–1682. [[CrossRef](#)]
52. Marrero-Lopez, D.; Pena-Martinez, J.; Ruiz-Morales, J.C.; Perez-Coll, D.; Aranda, M.A.G.; Nunez, P. Synthesis, phase stability and electrical conductivity of $\text{Sr}_2\text{MgMoO}_{6-\delta}$ anode. *Mater. Res. Bull.* **2008**, *43*, 2441–2450. [[CrossRef](#)]
53. Kong, L.; Liu, B.; Zhao, J.; Gu, Y.; Zhang, Y. Synthesis of nano-crystalline $\text{Sr}_2\text{MgMoO}_{6-\delta}$ anode material by a sol-gel thermolysis method. *J. Power Sources* **2009**, *188*, 114–117. [[CrossRef](#)]
54. Niakolas, D.K. Sulfur poisoning of Ni-based anodes for Solid Oxide Fuel Cells in H/C-based fuels. *Appl. Catal. A Gen.* **2014**, *486*, 123–142. [[CrossRef](#)]
55. Wang, W.; Su, C.; Wu, Y.; Ran, R.; Shao, Z. Progress in solid oxide fuel cells with nickel-based anodes operating on methane and related fuels. *Chem. Rev.* **2013**, *113*, 8104–8151. [[CrossRef](#)] [[PubMed](#)]

